Mon. Not. R. Astron. Soc. **000**, 1–16 (2014) Printed 17 February 2015 (MN LATEX style file v2.2)

A magnetic reconnection model for explaining the multi-wavelength emission of the microquasars Cyg X-1 and Cyg X-3

B. Khiali[1⋆], E. M. de Gouveia Dal Pino[1] and M. V. del Valle[2]
[1] *IAG-Universidade de São Paulo, Rua do Matão 1226, São Paulo, SP, Brazil*
[2] *Instituto Argentino de Radioastronomia (IAR), CCT La Plata, C.C.5, 1894 Villa Elisa, Buenos Aires, Argentina*

arXiv:1406.5664v4 [astro-ph.HE] 16 Feb 2015

17 February 2015

ABSTRACT
Recent studies have indicated that cosmic ray acceleration by a first-order Fermi process in magnetic reconnection current sheets can be efficient enough in the surrounds of compact sources. In this work, we discuss this acceleration mechanism operating in the core region of galactic black hole binaries (or microquasars) and show the conditions under which this can be more efficient than shock acceleration. In addition, we compare the corresponding acceleration rate with the relevant radiative loss rates obtaining the possible energy cut-off of the accelerated particles and also compute the expected spectral energy distribution (SED) for two sources of this class, namely Cygnus X-1 and Cygnus X-3, considering both leptonic and hadronic processes. The derived SEDs are comparable to the observed ones in the low and high energy ranges. Our results suggest that hadronic non-thermal emission due to photo-meson production may produce the very high energy gamma-rays in these microquasars.

Key words: Microquasars- cosmic ray acceleration: magnetic reconnection- radiation mechanisms: non-thermal.

1 INTRODUCTION

Detected non-thermal radio to gamma-ray emission from galactic binary systems hosting stellar mass black holes, also denominated black hole binaries (BHBs), microquasars, or simply μQSOs (Mirabel & Rodriquez 1994; Tingay et al. 1995; Hjellming & Rupen 1995), provide clear evidence of the production of relativistic particles in their jets and probably also in the innermost regions very close to the black hole (BH). Currently, more than a dozen microquasars have been detected in the galaxy (Zhang 2013).

Generally, these sources are far from being stable and individual systems have often complex emission structure. Nevertheless, all classes of BHBs exhibit common features and show basically two major states when considering their X-ray emission (2-100 keV): a quiescent and an outburst state (e.g., Remillard & McClintock 2006). The former is characterized by low X-ray luminosities and hard non-thermal spectra. Usually, transient BHBs exhibit this state for long periods, which allows one to obtain typical physical parameters of the system. On the other hand, the outburst state corresponds to intense activity and emission, and can be sub-classified in three main active and many intermediary states. According to Remillard & McClintock 2006 (see also Zhang 2013), the three main active states are the thermal state (TS), the hard state (HS) and the steep power law state (SPLS). These states are usually explained as changes in the structure of the accretion flow, as remarked before. During the TS, the soft X-ray thermal emission is believed to come from the inner region of the thin accretion disk that extends until the last stable orbits around the black hole. On the other hand, during the HS the observed weak thermal component suggests that the disk has been truncated at a few hundreds/thousands gravitational radii. The hard X-ray emission measured during this state is dominated by a power-law (PL) component and is often attributed to inverse Compton scattering of soft photons from the outer disk by relativistic electrons in the hot inner region of the system (e.g., Remillard & McClintock 2006; Malzak et al. 2006). The SPLS is almost a combination of the above two states, but the PL is steeper.

The observed radio and infra-red (IR) emission in microquasars is normally interpreted as due to synchrotron radiation produced by relativistic particles in the jet outflow.

More recently a few microquasars have been also detected in the gamma-ray range with *AGILE* (Tavani et al. 2009; Bulgarelli et al. 2010; Sabatini et al. 2010a,b, 2013), *Fermi-LAT* (Atwood et al. 2009; Bodaghee 2013) and

⋆ E-mail: bkhiali@usp.br

MAGIC (Lorentz 2004). For Cygnus X-1 (Cyg X-1), for instance, upper limits with 95% confidence level have been obtained in the range of $\geq$ 150 GeV (Albert et al. 2007), while in the case of Cygnus X-3 (Cyg X-3), upper limits of integrated gamma-ray flux above 250 GeV have been inferred by Aleksic et al. (2010). Upper limits in the 0.1-10 GeV range have been also suggested for GRS 1915+105 and GX 339-4.

There is no definite mechanism yet to explain the origin of the very high energy (VHE) emission in microquasars. The main reason for this is that the current sensitivity of the gamma-ray instruments is too poor to establish the location of this emission in the source (e.g., Bodaghee 2013).

Regardless of the uncertainties, several models have been proposed, especially for Cyg X-1 and Cyg X-3. Romero et al. 2003, for instance, assumed that the gamma-ray emission is produced in a hadronic jet as a result of the decay of neutral pions created in photon-ion collisions. An alternative model developed by Bosch-Ramon et al. 2005b assumed that relativistic protons also produced in the jet may diffuse through the interstellar medium (ISM) and then interact with molecular clouds and produce gamma-rays out of *pp* interactions via neutral pion decay. Another model has been proposed by Piano et al. 2012 in which both, leptonic (via inverse Compton) and hadronic (via neutral pion decay) might account for the observed gamma-ray emission.

All models above postulate that the primary relativistic particles (electrons and protons) are produced behind shocks in the jet outflow.

An alternative mechanism has been explored first in the context of microquasars (de Gouveia Dal Pino & Lazarian 2005, hereafter GL05) and later extended to the framework of active galactic nuclei (AGNs) (de Gouveia Dal Pino et al. 2010a, hereafter GPK10) in which particles are accelerated in the surrounds of the BH of these sources, near the jet basis, by a first-order Fermi process, as proposed in GL05, within magnetic reconnection current sheets produced in $fast$ encounters of the field lines arising from the accretion disk and those of the BH magnestosphere.

Fast magnetic reconnection, which occurs when two magnetic fluxes of opposite polarity encounter each other and partially annihilate very efficiently at a speed V_R of the order of the local Alfvén speed (V_A), has been detected in laboratory plasma experiments (e.g., Yamada et al. 2010) as well as in space environments, like the earth magnetotail and the solar corona (see e.g., Deng & Matsumoto 2001; Su et al. 2013). Extensive numerical work has been also carried out considering collisionless (e.g., Zenitani & Hoshino 2001; Zenitani et al. 2009; Drake et al. 2006, 2010; Cerutti et al. 2013, 2014; Sironi & Spitkovsky 2014) and collisional flows (e.g., Kowal et al. 2009, 2012; Shibata & Tanuma 2001; Loureiro et al. 2007). Different processes such as kinetic plasma instabilities (Shay et al. 1998, 2004; Yamada et al. 2010), anomalous resistivity (e.g., Parker 1979; Biskamp et al. 1997; Shay et al. 2004), or turbulence (Lazarian & Vishniac 1999, hereafter LV99, Kowal et al. 2009; Eyink et al. 2011), can lead to fast reconnection. The latter process in particular, has been found to be very efficient because it provokes the wandering of the magnetic field lines allowing for several simultaneous events of reconnection within the current sheet (see §2.2).

Fast reconnection has recently gained increasing interest also in other astrophysical contexts beyond the solar system because of its potential efficiency to explain magnetic field diffusion, dynamo process, and particle acceleration in different classes of sources and environments - from compact objects, like BHs (e.g., GL05, GL10, Giannios 2010), pulsars (e.g., Cerutti et al. 2013, 2014; Sironi & Spitkovsky 2014), and gamma ray bursts (e.g., Zhang & Yan 2011), to more diffuse regions like the interstellar medium (ISM), intergalactic medium (IGM), and star forming regions (e.g., Santos-Lima et al. 2010, 2012, 2013; Leão et al. 2013; see also Uzdensky 2011; de Gouveia Dal Pino & Kowal 2015; de Gouveia Dal Pino et al. 2014 and references therein for reviews).

In the mechanism proposed by GL05, particles are accelerated to relativistic velocities within the fast magnetic reconnection sheet in a similar way to the first-order Fermi process that occurs in shocks, i.e., trapped charged particles may bounce back and forth several times and gain energy due to head-on collisions with the two converging magnetic fluxes of opposite polarity (see §2.3). This acceleration mechanism has been also successfully tested numerically both in collisionless by means of two-dimensional (2D) PIC simulations (e.g., Drake et al. 2006; Zenitani & Hoshino 2001; Zenitani et al. 2009; Drake et al. 2010; Cerutti et al. 2013, 2014; Sironi & Spitkovsky 2014) and collisional magnetic reconnection sheets by means of 2D and 3D MHD simulations with test particles (Kowal et al. 2011, 2012). Furthermore, this process has been explored in depth in the natural laboratories of fast reconnection provided by solar flares (e.g., Drake et al. 2006; Lazarian & Opher 2009; Drake et al. 2010; Gordovskyy et al. 2010; Gordovskyy & Browning 2011; Zharkova et al. 2011) and the earth magnetotail. For instance, Lazarian & Opher (2009) verified that the anomalous cosmic rays measured by Voyager seem to be indeed accelerated in the reconnection regions of the magnetopause (see also Drake et al. 2010). In another study, Lazarian & Desiati (2010) invoked the same mechanism to explain the excess of cosmic rays in the sub-TeV and multi-TeV ranges in the wake produced as the Solar system moves through interstellar gas. Magnetic reconnection has been also invoked in the production of ultra high energy cosmic rays (e.g., Kotera & Olinto 2011) and in particle acceleration in astrophysical jets and gamma-ray bursts(Giannios 2010; del Valle et al. 2011; Zhang & Yan 2011).

In the context of BHs, GPK10 found that the energy power extracted from events of fast magnetic reconnection between the magnetosphere of the BH and the lines rising from the inner accretion disk can be more than sufficient to accelerate primary particles and produce the observed core radio synchrotron radiation from microquasars and low luminosity AGNs (LLAGNs). Moreover, they proposed that the observed correlation between the radio emission and the BH mass of these sources, spanning 10^{10} orders of magnitude in mass (in the so called fundamental plane of BHs, Merloni et al. 2003), might be related to this process. More recently, Kadowaki, de Gouveia Dal Pino & Singh 2014 (Kadowaki et al. 2015, henceforth KGS14) revisited this model exploring different mechanisms of fast magnetic reconnection and extended the study to include also the gamma-ray emission of a much larger sample containing over two hundred sources. They found that both LLAGNs and microquasars confirm the earlier trend found by GL05 and GPK10. Furthermore, when driven by turbulence, not only the radio but

also the gamma-ray emission of these sources can be due to the magnetic power released by fast reconnection allowing for particle acceleration to relativistic velocities in the core region of these sources. In another concomitant work Singh et al. 2015 (hereafter SGK14), have repeated the analysis above of KGS14, but instead of employing the standard accretion disk/coronal model to describe the BH surrounds, they adopted an MADAF (magnetically advected accretion flow) and obtained very similar results to those of KGS14, for the same large sample of LLAGNs and microquasars.

In addition, it has been argued in these studies that the fast magnetic reconnection events could be directly related to the transition between the hard and the soft steep-power-law (SPLS) X-ray states seen in microquasars, as described above.

Lately, similar mechanisms involving magnetic activity, reconnection and acceleration in the core regions of compact sources to explain their emission spectra have been also invoked by other works (e. g., Lyubarsky & Liverts 2008; Igumenshchev 2009; Soker 2010; Uzdensky & Spitkovsky 2014; Huang et al. 2014). In particular, magnetic reconnection between the magnetospheric lines of the central source and those anchored into the accretion disk resulting in the ejection of plasmons has been detected in numerical MHD studies by (see, e.g., Romanova et al. 2002, 2011; Zanni & Ferreira 2009, 2013; Čemeljić et al. 2013). The recent numerical relativistic MHD simulations of magnetically arrested accretion disks by Tchekhovskoy et al. 2011; McKinney et al. 2012; Dexter et al. 2014 also evidence the development of magnetic reconnection in the magnetosphere of the BH and are consistent with our scenario above.

The results above, and specially the correlations found in the works of KGS14 and SGK14 between the magnetic reconnection power released by turbulent driven fast reconnection in the surrounds of BHs and the observed core radio and gamma-ray emission of a sample containing more than 200 sources of microquasars and LLAGNS (see figures 7 in KGS14 and 3 in SGK14), have motivated us to perform the present study, undertaking a detailed multifrequency analysis of the non-thermal emission of two well investigated observationally microquasars, namely Cyg X-1 and Cyg X-3 (which are also in the KGS14 and SGK14 samples), aiming at reproducing their observed spectral energy distribution (SED) from radio to gamma-rays during outburst states. As in GL05, GPK10, KGS14 and SGK14, we explore the potential effects of the interactions between the magnetosphere of the BH and the magnetic field lines that rise from the accretion disk. These magnetic fields are considered essential ingredients in most accretion disk/BH models to help to explain the variety and complexity of observed data (e.g., Zhang 2013; Neronov & Aharonian 2007), but are, in general, paradoxically neglected or avoided in the discussion of the acceleration and emission mechanisms in the nuclear regions of these compact sources.

We here compute the power released by fast magnetic reconnection between these two magnetic fluxes and then the resulting particle spectrum of accelerated particles in the magnetic reconnection site. In particular, we explore the first-order Fermi acceleration process that may occur within the current sheet as proposed in GL05.

We finally consider the relevant radiative loss mechanisms due to the interactions of the accelerated particles with the ambient matter, magnetic and radiation fields, and also assess the importance of the acceleration by magnetic reconnection in comparison to shock acceleration.

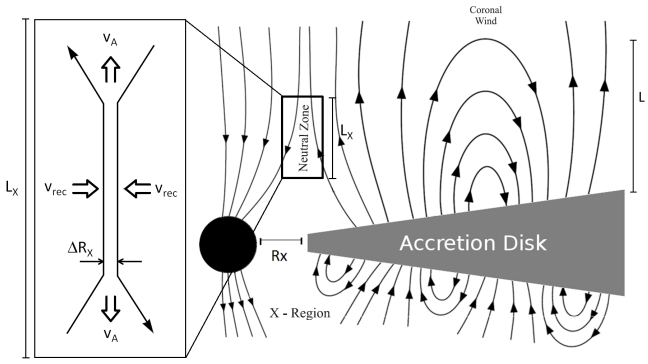

Figure 1. Scheme of magnetic reconnection between the lines rising from the accretion disk and the lines anchored into the BH horizon. Particle acceleration may occur in the magnetic reconnection site (neutral zone) by a first order Fermi process (adapted from GL05).

The outline of the paper is as follows. In Section 2, we describe in detail our acceleration model, while the equations employed to calculate the emission processes from radio to gamma-ray energies are presented in section 3. In Sections 4 and 5, we show the results of the application of the acceleration and emission model to Cyg X-1 and Cyg X-3, respectively. Finally in Section 6, we summarize our results and draw our conclusions.

2 OUR PARTICLE ACCELERATION SCENARIO

We assume here that relativistic particles may be accelerated in the core of the microquasar in the surrounds of the BH, near the basis of the jet launching region, as a result of events of fast magnetic reconnection. As stressed, this acceleration model has been described in detail in GL05 and GPK10 and recently revisited in KGS14. We summarize here its main assumptions. As in these former studies, we assume that the inner region of the accretion disk/corona system alternates between two states which are controlled by changes in the global magnetic field. Right before a fast magnetic reconnection event, we assume that the system is in a state that possibly characterizes the transition from the hard to the soft state as described in the previous section, and adopt a magnetized accretion disk with a corona around the BH.

2.1 The accretion disk/coronal fluid around the BH

Although there is still much speculation on what should be the strength and geometry of the magnetic fields in the surrounds of BHs, these are necessary ingredients in order to explain, e.g., the formation of narrow relativistic jets. We consider here a scenario with the simplest possible configuration by considering a magnetized standard (geometrically thin and optically thick) accretion disk around the BH as in the cartoon of Fig. 1.

A magnetosphere around the central BH can be established from the drag of magnetic field lines by the accretion disk. The large-scale poloidal magnetic field in the disk corona can in turn be formed by the action of a turbulent dynamo inside the accretion disk (see GL05, KGL14 and references therein) or dragged from the surroundings. This poloidal magnetic flux under the action of the disk differential rotation gives rise to a wind that partially removes angular momentum from the system and increases the accretion rate. This also increases the ram pressure of the accreting material that will then press the magnetic lines in the inner disk region against the lines anchored into the BH horizon allowing them to reconnect fast (see Figure 1). Momentum flux conservation between the magnetic pressure of the BH magnetosphere and the accreting flux determines the magnetic field intensity in this inner region.

2.2 Conditions for fast reconnection in the surrounds of the BH

As discussed in §1 (see also GL05, GPK10, and KGS14), in the presence of kinetic plasma instabilities (Shay et al. 1998, 2004; Yamada et al. 2010), anomalous resistivity (e.g., Parker 1979; Biskamp et al. 1997; Shay et al. 2004), or turbulence (Lazarian & Vishniac 1999; Kowal et al. 2009, 2012), reconnection may become very efficient and fast.

The strongly magnetized and low dense coronal fluid of the systems we are dealing with in this work satisfies the condition $L > l_{mfp} > r_l$ (where L is the typical large scale dimension of the system, l_{mfp} the ion mean free path and r_l the ion Larmor radius). For such flows a weakly collisional or effectively collisional MHD description is more than appropriate (e.g. Liu et al. 2003) and we will employ this approach here, as in GL05, GPK10, and KGS14[1]

In these MHD flows, a collisional turbulent fast reconnection approach is expected to be dominant (see KGL14). According to the LV99 model, the presence of even weak turbulence causes the wandering of the magnetic field lines which allows for many independent patches to reconnect simultaneously making the global reconnection rate large, $V_R \sim v_A(l_{inj}/L)^{1/2}(v_{turb}/v_A)^2$, where V_R is the reconnection speed, and l_{inj} and v_{turb} the injection scale and velocity of the turbulence, respectively. This expression indicates that the reconnection rate can be as large as $\sim V_A$, which in the systems here considered may be near the light speed (see also KGL14). This theory has been extensively investigated (e.g. Eyink et al. 2011; Lazarian et al. 2012) and confirmed numerically by means of 3D MHD simulations (Kowal et al. 2009, 2012). In particular, it has been shown (Eyink et al. 2011) that turbulent collisional fast reconnection prevails when the thickness of the current sheet (see eq. 4 below) is larger than the ion Larmor radius. As demonstrated in KGS14, for the systems we are studying this condition is naturally satisfied and we will adopt this model to derive the magnetic power released by fast reconnection. [2]

The employment of a fast magnetic reconnection model driven by turbulence as in LV99 requires fiducial sources of turbulence. The fluid in these sources, as most astrophysical fluids, has large Reynolds numbers. In fact, $R_e = LV/\nu \sim 10^{20}$ (where V corresponds to a characteristic velocity of the fluid and ν is the kinematic viscosity which for a magnetized fluid is dominated by transverse kinetic motions to the magnetic field and is given by $\nu \sim 1.7 \times 10^{-2} n_c ln\Lambda/(T^{0.5}B^2)$ cm^{2}s^1, being $ln\Lambda \sim 25$ the Coulomb logarithm and n_c is the coronal particle number density given by eq. 3 below). Likewise, the magnetic Reynolds number is $R_{em} = LV/\eta \sim 10^{18}$ (where the magnetic diffusion coefficient η in the regime of strong magnetic fields is given by $\eta = 1.3\times10^{13} cm^2 s^1 Z ln\Lambda T^{-3/2}$ (Spitzer 1962). As argued in KGL14, such high Reynolds numbers imply that both the fluid and the magnetic field lines can be highly distorted and turbulent if there is turbulence triggering. In other words, any instability as for instance, current driven instabilities, can naturally drive turbulence with characteristic velocities around the particles thermal speed. Also, the occurrence of continuous magnetic reconnection during the building of the corona itself in the surrounds of the BH (Liu et al. 2003) will contribute to the onset of turbulence which will then be further fed by fast reconnection as in LV99 model. Numerical simulations of coronal disk accretion also indicate the formation of turbulent flow in the surrounds of the BH that may be triggered by magnetorotational instability (see e.g, Tchekhovskoy et al. 2011; McKinney et al. 2012; Dexter et al. 2014). All these processes may ensure the presence of embedded turbulence in the magnetic discontinuity described in Figure 1.

We should also note that in the equations below which describe the accreting and coronal flow around the BH, we adopt a nearly non relativistic approximation. In KGS14, we give quantitative arguments that indicate that this is a reasonable assumption. For instance, the evaluation of the magnetic reconnection power considering a pseudo-Newtonian gravitational potential to reproduce general relativistic effects, gives a value that is similar to the classical case. A kinematic relativistic approach for the accreting and coronal flows is not necessary either since we are dealing with characteristic ion/electron temperatures smaller than or equal $\sim 10^9$K (see KGS14). Nevertheless, with regard to reconnection, the fact that v_A may approach the light speed, may imply that relativistic effects can affect the turbulent driven fast reconnection. This question has been addressed in some

[1] We should further notice that the BH of these systems is surrounded by accreting flow from the stellar companion which also favours a nearly collisional MHD approach.

[2] It should be noticed that GL05, GPK10 and KGS14 have also investigated another mechanism to induce fast magnetic reconnection based on anomalous resistivity (AR). This occurs in the presence of current driven instabilities that can enhance the microscopic Ohmic resistivity and speed up reconnection to rates much larger than that probed by the latter. On the other hand, AR results rates which are much smaller than reconnection driven by turbulence as it prevails only at very small scales of the fluid. In fact, as shown in KGL14, AR predicts a much thinner reconnection region and is unable to reproduce the observed emission for most of the sources investigated. In particular, in the case of Cyg X-1 and Cyg X-3, the magnetic power released by fast reconnection driven by AR cannot accelerate particles to energies larger than 10^{12} eV (see more details in KGS14). Other instabilities, like e.g., tearing mode or Hall effect are also relevant to drive fast reconnection but only at very small scales as well, and are thus more appropriate for collisionless fluids (see Eyink et al. 2011).

detail in KGL14 as well, and we refer to this work (and the references therein). The current results indicate that one can treat both cases in a similar way. In particular, a recent study (Cho & Lazarian 2014) has demonstrated that relativistic collisional MHD turbulence behaves as in the non-relativistic case which indicates that LV99 theory can be also applicable in the nearly relativistic regime.

Considering the assumptions above, KGS14 have demonstrated that the magnetic power released by a fast magnetic reconnection event driven by turbulence in the corona around the BH, is given by:

$$W \simeq 1.66 \times 10^{35} \Gamma^{-0.5} r_X^{-0.62} l^{-0.25} l_X q^{-2} \xi^{0.75} m \ \ \mathrm{erg\ s^{-1}}, \quad (1)$$

Where $r_X = R_X/R_S$ is the inner radius of the accretion disk in units of the BH Schwartzchild radius (R_S) (as in KGS14, in our calculations we assume $r_X = 6$); $l = L/R_S$ is the height of the corona in units of R_S; $l_X = L_X/R_S$ where L_X is the extension of the magnetic reconnection zone (as shown in Figure 1; see also Tables 1 and 2); $q = [1-(3/r_X)^{0.5}]^{0.25}$; ξ is the mass accretion disk rate in units of the Eddington rate ($\xi = \dot{M}/\dot{M}_{Edd}$) which we assume to be $\xi \simeq 0.7$[3]; m is the BH mass in units of solar mass, and $v_A = v_{A0}\Gamma$, is the relativistic form of the Alfvén velocity, with $v_{A0} = B/(4\pi\rho)^{1/2}$, B being the local magnetic field, ρ the fluid density, and $\Gamma = [1 + (\frac{v_{A0}}{c})^2]^{-1/2}$ (Somov 2012). In this work, $v_{A0} \sim c$ (see below).

The ambient magnetic field in the surrounds of the BH calculated from the GL05 and KGS14 model is given by:

$$B \cong 9.96 \times 10^8 r_X^{-1.25} \xi^{0.5} m^{-0.5} \ \mathrm{G}. \quad (2)$$

The particle density in the coronal region in the surrounds of the BH is

$$n_c \cong 8.02 \times 10^{18} r_X^{-0.375} \Gamma^{0.5} l^{-0.75} q^{-2} \xi^{0.25} m^{-1} \ \mathrm{cm^{-3}}. \quad (3)$$

The equations above will be employed in Sections 4 and 5 to model the acceleration in the core region of the microquasars Cyg X-1 and Cyg X-3. The acceleration region in our model is taken to be the cylindrical shell where magnetic reconnection takes place, as in Figure 1. This shell has a length l_X, and inner and outer radii R_X and $R_X + \Delta R_X$ respectively, where ΔR_X is the width of the current sheet given by (KGS14):

$$\Delta R_X \cong 2.34 \times 10^4 \Gamma^{-0.31} r_X^{0.48} l^{-0.15} l_X q^{-0.75} \xi^{-0.15} m \ \mathrm{cm}. \quad (4)$$

In sections 4 and 5, we will also need the accretion disk temperature in order to evaluate its black body radiation field:

$$T_d \cong 3.71 \times 10^7 \alpha^{-0.25} r_X^{-0.37} m^{0.25} \ \mathrm{K}, \quad (5)$$

where $0.05 \leq \alpha < 1$ is the Shakura-Sunyaev disk viscosity parameter which we here assume to be of the order of 0.5.

[3] We note that according to the results of KGS14 (see their Figure 5), accretion rates ξ between $0.05 < \xi \leq 1$ are able to produce magnetic reconnection power values which are large enough to probe the observed luminosities from microquasars. We here adopted $\xi \simeq 0.7$ as a fiducial value.

2.3 Particle acceleration due to the magnetic energy released by fast reconnection

The magnetic power released by a fast reconnection event heats the surrounding gas and may accelerate particles. We assume that approximately 50% of the reconnection power is used to accelerate the particles. This is consistent with recent plasma laboratory experiments of particle acceleration in reconnection sheets (e.g., Yamada et al. 2014) and also with solar flare observations where up to 50% of the released magnetic energy appears in the form of energetic electrons (e.g., Lin & Hudsun 1971).

As in shock acceleration where particles confined between the upstream and downstream flows undergo a first-order Fermi acceleration, GL05 proposed that a similar mechanism would occur when particles are trapped between the two converging magnetic flux tubes moving to each other in a magnetic reconnection current sheet with a velocity V_R. They showed that, as particles bounce back and forth due to head-on collisions with magnetic fluctuations in the current sheet, their energy after a round trip increases by $< \Delta E/E > \sim 8V_R/3c$, which implies a first-order Fermi process with an exponential energy growth after several round trips (GL05; see also de Gouveia Dal Pino & Kowal 2015). Under conditions of $fast$ magnetic reconnection V_R is of the order of the local Alfvén speed V_A, at the surroundings of relativistic sources, $V_R \simeq v_A \simeq c$ and thus the mechanism can be rather efficient (GL05, Giannios 2010).

As remarked earlier, this mechanism has been thoroughly tested by means of 3D MHD numerical simulations in which charged thermal particles are accelerated to relativistic energies into collisional domains of fast magnetic reconnection without including kinetic effects (Kowal et al. 2011, 2012).[4]

Using the results of the 3D MHD numerical simulations of the acceleration of test particles in current sheets where reconnection was made fast by embedded turbulence (Kowal et al. 2012), we find that the acceleration rate for a proton is given by:

$$t_{acc,rec,p}^{-1} = 1.3 \times 10^5 \left(\frac{E}{E_0}\right)^{-0.4} t_0^{-1}, \quad (6)$$

where E is the energy of the accelerated proton, $E_0 = m_p c^2$, m_p is the proton rest mass, $t_0 = l_{acc}/v_A$ is the Alfvén time,

[4] We note also that tests performed in collisionless fluids, by means of 2D (e.g. Zenitani & Hoshino 2001; Zenitani et al. 2009; Drake et al. 2006, 2010; Cerutti et al. 2013, 2014; Sironi & Spitkovsky 2014), and 3D PIC simulations (Sironi & Spitkovsky 2014) have generally achieved similar results to those of collisional studies with regard to acceleration rates and particle power law spectra, with the only difference that these can probe only the kinetic scales of the process, while the collisional MHD simulations probe large scales (Kowal et al. 2011, 2012). In particular, Kowal et al. (2011) have demonstrated by means of 2D and 3D collisional MHD simulations the equivalence between first-order Fermi particle acceleration involving 2D converging magnetic islands in current sheets, which arise in collisionless fluid simulations (e.g., Drake et al. 2006, 2010), and the same process in 3D reconnection sites where the islands naturally break out into loops. Kowal et al. (2011) further demonstrated the importance of the presence of guide fields in 2D simulations to ensure equivalence with the results of more realistic 3D particle acceleration simulations.

and l_{acc} is the length scale of the acceleration region. Although this result was found from numerical simulations employing protons as test particles, we can derive a similar expression for the electrons:

$$t^{-1}_{acc,rec,e} = 1.3 \times 10^5 \sqrt{\frac{m_p}{m_e}} \left(\frac{E}{E_0}\right)^{-0.4} t_0^{-1}, \quad (7)$$

where m_e is the electron rest mass.

The equations above will be used to compute the acceleration rates in our model as described in the following sections.

The accelerated particles develop a power law energy distribution (see also Appendix A):

$$Q(E) \propto E^{-p}, \quad (8)$$

we assume for the power law index $p = 1.8$ and $p = 2.2$ for Cyg X-1 and Cyg X-3, respectively, which are compatible with the predicted values in analytical and numerical studies (GL05, Drury 2012; de Gouveia Dal Pino & Kowal 2015; del Valle et al. 2015).[5]

As stressed in GL05, it is also possible that a diffusive shock may develop in the surrounds of the magnetic reconnection zone, at the jet launching region, due to the interaction of "coronal mass ejections", which are released by fast reconnection along the magnetic field lines, just like, e.g., in the Sun. A similar picture has been also suggested by e.g., Romero et al. (2010b). In this case, one should expect the shock velocity to be predominantly parallel to the magnetic field lines and the acceleration rate for a particle of energy E in a magnetic field B, will be approximately given by (e.g., Spruit 1988):

$$t^{-1}_{acc,shock} = \frac{\eta e c B}{E}, \quad (9)$$

where $0 < \eta \ll 1$ characterizes the efficiency of the acceleration. We fix $\eta = 10^{-2}$, which is appropriate for shocks with velocity $v_s \approx 0.1c$ commonly assumed in the Bohm regime (Romero et al. 2010b) (see further discussion in Section 6).

The accelerated particles lose their energy radiatively via interactions with the surrounding magnetic field (producing synchrotron emission), the photon field (producing inverse Compton, synchrotron-self-Compton, and photomesons $p\gamma$), and with the surrounding matter (producing pp collisions and relativistic Bremsstrahlung radiation).

In the following section we discuss the relevant radiative loss processes for electrons and protons which will allow the construction of the SED of these sources for comparison with the observations.

3 EMISSION AND ABSORPTION MECHANISMS

3.1 Interactions with magnetic field

Charged particles with energy E, mass m and charge number Z spiralling in a magnetic field $\vec{B}$ emit synchrotron radiation at a rate

$$t^{-1}_{synch}(E) = \frac{4}{3}\left(\frac{m_e}{m}\right)^3 \frac{\sigma_T B^2}{m_e c 8\pi} \frac{E}{mc^2}, \quad (10)$$

where m_e is the electron mass and σ_T is the Thompson cross section. The synchrotron spectrum radiated by a distribution of particles $N(E)$ (see appendix A) as function of the scattered photon energy (E_γ) (in units of power per unit area) is

$$L_\gamma(E_\gamma) = \frac{E_\gamma V_{vol}}{4\pi d^2} \frac{\sqrt{2} e^3 B}{hmc^2} \int_{E_{min}}^{E_{max}} dE N(E) \frac{E_\gamma}{E_c} \int_{\frac{E_\gamma}{E_c}}^{\infty} K_{5/3}(\xi) d\xi, \quad (11)$$

where V_{vol} is the volume of the emission region, d is the distance of the source from us, h is the Planck constant, $K_{5/3}(\xi)$ is the modified Bessel function of 5/3 order, and the characteristic energy E_c is

$$E_c = \frac{3}{4\pi} \frac{ehB}{mc} \left(\frac{E}{mc^2}\right)^2. \quad (12)$$

In these calculations we assumed that the particle velocity is perpendicular to the local magnetic field.

To compute equation (11) we used the approximation

$$x \int_x^\infty K_5/3(\xi) d\xi \approx 1.85 x^{1/3} e^{-x}. \quad (13)$$

Practically, the synchrotron emission of the electrons dominates the low energy photon background which is a proper target for both inverse Compton (IC) and $p\gamma$ interactions (see below; see also Reynoso, Medina & Romero 2011). The number density for multi-wavelength synchrotron scattered photons (in units of energy per volume), has been approximated as (Zhang, Chen & Fang 2008)

$$n_{synch}(\epsilon) = \frac{L_\gamma(\epsilon)}{\epsilon^2 V_{vol}} \frac{r}{c} 4\pi d^2, \quad (14)$$

where r stands for the radius of the emission region and ϵ for the scattered synchrotron radiation energy. More precisely, ϵ corresponds to the photon energy of the multi-wavelength target radiation field for SSC and $p\gamma$ interactions. The volume V_{vol} of the emission region in our model is taken as the spherical region that encompasses the cylindrical shell where magnetic reconnection particle acceleration takes place in Figure 1. Considering that the cylinder extends up to L, then $r \simeq L$ and the effective emission zone in our model has an approximate volume $4\pi L^3/3$ (see Tables 1 and 2).

[5] We note that analytical estimates of the first-order Fermi accelerated particle power law spectrum in current sheets predict power law indices $p \sim 1 - 2.5$ (e.g., GL05, Drury 2012; Giannios 2010), while 3D MHD numerical simulations with test particles predict $p \sim 1$ (Kowal et al. 2012 and see also the review by de Gouveia Dal Pino & Kowal 2015), which is comparable with results obtained from 2D collisionless PIC simulations considering merging islands $p \sim 1.5$ (Drake et al. 2010), or X-type Petschek 2D configurations (e.g., Zenitani & Hoshino 2001), for which it has been obtained $p \sim 1$, or even with more recent 3D PIC simulations (Sironi & Spitkovsky 2014) which obtained $p < 2$. In summary, considering both analytical and numerical predictions $p \sim 1 - 2.5$. However, at least in the case of the 3D MHD simulations, some caution is necessary with the derived spectral index $p \sim 1$, because in these simulations particles are allowed to re-enter in the periodic boundaries of the computational domain and be further accelerated causing some deposition of particles in the very high energy tail of the spectrum after saturation of the acceleration which may induce some artificial increase in the slope (del Valle et al. 2015).

3.2 Interactions with matter

3.2.1 Bremsstrahlung

When a relativistic electron accelerates in the presence of the electrostatic field of a charged particle or a nucleus of charge Ze, Bremsstrahlung radiation is produced. For a fully ionized plasma with ion number density n_i, the Bremsstrahlung cooling rate is (Berezinskii 1990):

$$t_{Br}^{-1} = 4n_i Z^2 r_0^2 \alpha_f c \left[\ln\left(\frac{2E_e}{m_e c^2}\right) - \frac{1}{3}\right], \quad (15)$$

where r_0 is the electron classical radius and α_f stands for the fine structure constant. The relativistic Bremsstrahlung spectrum (in units of power per unit area) is given by (Romero et al. 2010a)

$$L_\gamma(E_\gamma) = \frac{E_\gamma V_{vol}}{4\pi d^2} \int_{E_\gamma}^{\infty} n\sigma_B(E_e, E_\gamma) \frac{c}{4\pi} N_e(E_e) dE_e, \quad (16)$$

where

$$\sigma_B(E_e, E_\gamma) = \frac{4\alpha_f r_0^2}{E_\gamma} \Phi(E_e, E_\gamma), \quad (17)$$

and

$$\Phi(E_e, E_\gamma) = \left[1 + \left(1 - \frac{E_\gamma}{E_e}\right)^2 - \frac{2}{3}\left(1 - \frac{E_\gamma}{E_e}\right)\right] \times \left[\ln\frac{2E_e(E_e - E_\gamma)}{m_e c^2 E_\gamma} - \frac{1}{2}\right]. \quad (18)$$

3.2.2 pp interactions

One relevant gamma-ray production mechanism is the decay of neutral pions which can be created through inelastic collisions of the relativistic protons with nuclei of the corona that surrounds the accretion disk. In this case the cooling rate is given by (Kelner 2006)

$$t_{pp}^{-1} = n_i c \sigma_{pp} k_{pp}, \quad (19)$$

where k_{pp} is the total inelasticity of the process of value ~ 0.5. The corresponding cross section for inelastic *pp* interactions σ_{pp} can be approximately by (Kelner et al. 2009)

$$\sigma_{pp}(E_p) = \left(34.3 + 1.88L + 0.25L^2\right)\left[1 - \left(\frac{E_{th}}{E_p}\right)^4\right]^2 \text{mb}, \quad (20)$$

where mb stands for milli-barn, $L = \ln\left(\frac{E_p}{1TeV}\right)$, and the proton threshold kinetic energy for neutral pion (π^0) production is $E_{th} = 2m_\pi c^2(1 + \frac{m_\pi}{4m_p}) \approx 280$ MeV, where $m_\pi c^2 = 134.97$ MeV is the rest energy of π^0 (Vila & Aharonian 2009). This particle decays in two photons with a probability of 98.8%.

The spectrum can be calculated by

$$L_\gamma(E_\gamma) = \frac{E_\gamma^2 V_{vol}}{4\pi d^2} q_\gamma(E_\gamma), \quad (21)$$

where $q_\gamma(E_\gamma)(\text{erg}^{-1}\text{cm}^{-3}\text{s}^{-1})$ is the gamma-ray emissivity.

For proton energies less than 0.1 TeV, $q_\gamma(E_\gamma)$ is

$$q_\gamma(E_\gamma) = 2\int_{E_{min}}^{\infty} \frac{q_\pi(E_\pi)}{\sqrt{E_\pi^2 - m_\pi^2 c^4}} dE_\pi, \quad (22)$$

where $E_{min} = E_\gamma + m_\pi^2 c^4/4E_\gamma$ and $q_\pi(E_\pi)$ is the pion emissivity. An approximate expression for $q_\pi(E_\pi)$ can be calculated using the δ-function (Aharonian & Atoyan 2000). For this purpose, a fraction k_π of the kinetic energy of the proton $E_{kin} = E_p - m_p c^2$ is taken by the neutral pion(Vila & Aharonian 2009). The neutral pion emissivity is then given by

$$q_\pi(E_\pi) = cn_i \int \delta(E_\pi - k_\pi E_{kin}) \sigma_{pp}(E_p) N_p(E_p) dE_p = \frac{cn_i}{k_\pi} \sigma_{pp}(m_p c^2 + \frac{E_\pi}{k_\pi})\, N_p(m_p c^2 + \frac{E_\pi}{k_\pi}). \quad (23)$$

The target ambient nuclei density is given by n_i and $N_p(E_p)$ stands for the energy distribution of the relativistic protons.

For proton energies in the range GeV-TeV, $k_\pi \approx 0.17$ (Gaisser 1990), the total cross section $\sigma_{pp}(E_p)$ can be approximated by

$$\sigma_{pp}(E_p) \approx \begin{cases} 30\left[0.95 + 0.06 ln\left(\frac{E_{kin}}{1GeV}\right)\right] mb & E_{kin} \geq 1\text{GeV}, \\ 0 & E_{kin} < 1\text{GeV}. \end{cases} \quad (24)$$

For proton energies greater than 0.1 TeV, the gamma-ray emissivity is

$$q_\gamma(E_\gamma) = cn_i \int_{E_\gamma}^{\infty} \sigma_{inel}(E_p) N_p(E_p) E_\gamma(\frac{E_\gamma}{E_p}, E_p) \frac{dE_p}{E_p} = cn_i \int_0^1 \sigma_{inel}(\frac{E_\gamma}{x}) N_p(\frac{E_\gamma}{x}) F_\gamma(x, \frac{E_\gamma}{x}) \frac{dx}{x}. \quad (25)$$

The inelastic *pp* cross section is approximately given by

$$\sigma_{inel}(E_p) = (34.3 + 1.88L + 0.25L^2)[1 - (\frac{E_{th}}{E_p})^4]^2 mb, \quad (26)$$

Here $E_{th} = m_p + 2m_\pi + \frac{m_\pi^2}{2m_p} = 1.22$ GeV is the threshold energy of the proton to produce neutral pions π^0 and the number of photons whose energies are in the range of $(x, x + dx)$ where $x = E_\gamma/E_p$, caused per *pp* collision can be approximated by (Vila & Aharonian 2009)

$$F_\gamma(x, E_p) = B_\gamma \frac{lnx}{x} [\frac{1 - x^{\beta_\gamma}}{1 + k_\gamma x^{\beta_\gamma}(1 - x^{\beta_\gamma})}]^4 \times [\frac{1}{lnx} - \frac{4\beta_\gamma x^{\beta_\gamma}}{1 - x^{\beta_\gamma}} - \frac{4k_\gamma \beta_\gamma x^{\beta_\gamma}(1 - 2x^{\beta_\gamma})}{1 + k_\gamma x^{\beta_\gamma}(1 - x^{\beta_\gamma})}]. \quad (27)$$

The best least-squares fits to the numerical calculations yield:

$$B_\gamma = 1.30 + 0.14L + 0.011L^2, \quad (28)$$

$$\beta_\gamma = (1.79 + 0.11L + 0.008L^2)^{-1}, \quad (29)$$

$$k_\gamma = (0.801 + 0.049L + 0.014L^2)^{-1}. \quad (30)$$

Where $L = ln(E_p/1TeV)$ and $0.001 \leq x \leq 0.1$ (for more details see Vila & Aharonian 2009).

3.3 Interactions with the radiation field

Energetic electrons transfer their energy to low energy photons causing them to radiate at high energies (inverse Compton process). On the other hand, when high energy protons

interact with low energy photons ($p\gamma$ interactions) they produce pions and gamma-ray photons with energies larger than 10^8 eV in the so called photomeson process.

3.3.1 Inverse Compton

The IC cooling rate for an electron in both Thomson and Klein-Nishina regimes is given by (Blumenthal & Gould 1970)

$$t_{IC}^{-1}(E_e) = \frac{1}{E_e}\int_{\epsilon_{min}}^{\epsilon_{max}}\int_{E_{ph}}^{\frac{\Gamma E_e}{1+\Gamma}}(E_\gamma - E_{ph})\frac{dN}{dtdE_\gamma}dE_\gamma. \quad (31)$$

Here E_{ph} and E_γ are the incident and scattered photon energies, and

$$\frac{dN}{dtdE_\gamma} = \frac{2\pi r_0^2 m_e^2 c^5}{E_e^2}\frac{n_{ph}(E_{ph})dE_{ph}}{E_{ph}}F(q), \quad (32)$$

where $n_{ph}(E_{ph})$ is the target photon density (in the units of energy^{-1}volume^{-1}) and

$$F(q) = 2q\ln q + (1+2q)(1-q) + 0.5(1-q)\frac{(\Gamma q)^2}{1+\Gamma}, \quad (33)$$

$$\Gamma = 4E_{ph}E_e/(m_e c^2)^2, \quad (34)$$

$$q = \frac{E_\gamma}{[\Gamma(E_e - E_\gamma)]}. \quad (35)$$

Accelerated electrons may have interaction with photons produced by the synchrotron emission in the coronal region (eq. 14), in which case the process is SSC, or by photons emitted by the surface of the accretion disk. This photon field can be represented by a black body radiation and is given by [6]

$$n_{bb}(E_{ph}) = \frac{1}{\pi^2\lambda_c^3 m_e c^2}(\frac{E_{ph}}{m_e c^2})^2[\frac{1}{\exp(\frac{E_{ph}}{kt})-1}]. \quad (36)$$

Here λ_c, t and k are the Compton wavelength, disk temperature and Boltzmann constant, respectively. We will see below that for the microquasars, the SSC will be dominating.

Taking into account the Klein-Nishina effect on the cross section, the total luminosity per unit area can be calculated from (Romero et al. 2010a)

$$L_{IC}(E_\gamma) = \frac{E_\gamma^2 V_{vol}}{4\pi d^2}\int_{E_{min}}^{E_{max}} dE_e N_e(E_e) \times \int_{E_{ph,min}}^{E_{ph,max}} dE_{ph} P_{IC}(E_\gamma, E_{ph}, E_e), \quad (37)$$

where $P_{IC}(E_\gamma, E_{ph}, E_e)$ is the spectrum of photons scattered by an electron of energy $E_e = \gamma_e m_e c^2$ in a target radiation field of density $n_{ph}(E_{ph})$. According to Blumenthal & Gould (1970), it is given by

$$P_{IC}(E_\gamma, E_{ph}, E_e) = \frac{3\sigma_t c(m_e c^2)^2}{4E_e^2}\frac{n_{ph}(E_{ph})}{E_{ph}}F(q), \quad (38)$$

and for the scattered photons there is a range which is

$$E_{ph} \le E_\gamma \le \frac{\Gamma}{1+\Gamma}E_e. \quad (39)$$

[6] We note that the contribution of target photons due to the radiation field produced by the companion star is found to be irrelevant in our model (e.g., Bosch-Ramon et al. 2005a).

3.3.2 Photomeson production ($p\gamma$)

The photomeson production takes place for photon energies greater than $E_{th} \approx 145$MeV. A single pion can be produced in an interaction near the threshold and then decay giving rise to gamma-rays. In our model the appropriate photons come from the synchrotron radiation. [7] The cooling rate for this mechanism in an isotropic photon field with density $n_{ph}(E_{ph})$ can be calculated by Stecker (1968):

$$t_{p\gamma}^{-1}(E_p) = \frac{c}{2\gamma_p^2}\int_{\frac{E_{th}^{(\pi)}}{2\gamma_p}}^{\infty} dE_{ph}\frac{n_{ph}(E_{ph})}{E_{ph}^2} \times \int_{E_{th}^{(\pi)}}^{2E_{ph}\gamma_p} d\epsilon_r \sigma_{p\gamma}^{(\pi)}(\epsilon_r)K_{p\gamma}^{(\pi)}(\epsilon_r)\epsilon_r, \quad (40)$$

where $\gamma_p = \frac{E_p}{m_e c^2}$, ϵ_r is the photon energy in the rest frame of the proton and $K_{p\gamma}^{(\pi)}$ is the inelasticity of the interaction. Atoyan & Dermer (2003) proposed a simplified approach to calculate the cross-section and the inelasticity which are given by

$$\sigma_{p\gamma}(\epsilon_r) \approx \begin{cases} 340\ \mu barn & 300\text{MeV} \le \epsilon_r \le 500\text{MeV} \\ 120\ \mu barn & \epsilon_r > 500\text{MeV}, \end{cases} \quad (41)$$

and

$$K_{p\gamma}(\epsilon_r) \approx \begin{cases} 0.2 & 300\text{MeV} \le \epsilon_r \le 500\text{MeV} \\ 0.6 & \epsilon_r > 500\text{MeV}. \end{cases} \quad (42)$$

To find the luminosity from the decay of pions, we use the analytical approach proposed by Atoyan & Dermer (2003). Taking into account that each pion decays into two photons, the $p\gamma$ luminosity is

$$L_{p\gamma}(E_\gamma) = 2\frac{E_\gamma^2 V_{vol}}{4\pi d^2}\int Q_{\pi^0}^{(p\gamma)}(E_\pi)\delta(E_\gamma - 0.5E_\pi)dE_\pi = 20\frac{E_\gamma^2 V_{vol}}{4\pi d^2}N_p(10E_\gamma)\omega_{p\gamma,\pi}(10E_\gamma)n_{\pi^0}(10E_\gamma), \quad (43)$$

where $Q_{\pi^0}^{(p\gamma)}$ is the emissivity of the neutral pions given by

$$Q_{\pi^0}^{(p\gamma)} = 5N_p(5E_\pi)\omega_{p\gamma,\pi}(5E_\pi)n_{\pi^0}(5E_\pi), \quad (44)$$

$\omega_{p\gamma}$ stands for the collision rate which is

$$\omega_{p\gamma}(E_p) = \frac{m_p^2 c^5}{2E_p^2}\int_{\frac{E_{th}}{2\gamma_p}}^{\infty} dE_{ph}\frac{n_{ph}(E_{ph})}{E_{ph}^2}\int_{E_{th}}^{2E_{ph}\gamma_p} dE_r \sigma_{p\gamma}^{(\pi)}(E_r)E_r, \quad (45)$$

and n_{π^0} is the mean number of neutral pions produced per collision given by

$$n_{\pi^0}(E_p) = 1 - P(E_p)\xi_{pn}. \quad (46)$$

In the single-pion production channel, the probability for the conversion of a proton to a neutron with the emission of a $\pi^+ - meson$ is given by $\xi_{pn} \approx 0.5$. For photomeson interactions of a proton with energy E_p, the interaction probability is represented by $P(E_p)$, which is

[7] We find that for photomeson production, the radiation from the accretion disk and from the companion star are irrelevant compared to the contribution from the synchrotron emission.

$$P(E_p) = \frac{K_2 - \bar{K}_{p\gamma}(E_p)}{K_2 - K_1}. \quad (47)$$

The inelasticity in the single-pion channel is approximated as $K_1 \approx 0.2$, whereas $K_2 \approx 0.6$. For energies above 500 MeV the mean inelasticity $\bar{K}_{p\gamma}$ is

$$\bar{K}_{p\gamma} = \frac{1}{t_{p\gamma}(\gamma_p)\omega_{p\gamma}(E_p)}. \quad (48)$$

3.4 Absorption

Gamma-rays can be annihilated by the surrounding radiation field via electron-positron pair creation: $\gamma+\gamma \rightarrow e^+ + e^-$. In microquasars, besides the radiation field of the tight companion star, coronal and accretion disk photons can also absorb $\gamma-$rays. However, it has been shown by Cerutti et al. (2011) that the absorption due to coronal photons is negligible compared with the contribution from the disk. Adopting the same absorption model for the disk radiation field of these authors we find that the disk contribution to gamma-ray absorption is less relevant than that of the stellar companion, generally a Wolf-Rayet star, which produces UV radiation. To evaluate the optical depth due to this component, we have adopted the model described by Sierpowska-Bartosik & Torres (2008), (see also Dubus 2006; Zdziarski & Mikolajewska 2013). This process is possible only above a kinematic energy threshold given by

$$E_\gamma \epsilon (1 - \cos\theta) \geq 2 m_e^2 c^4, \quad (49)$$

and

$$E_\gamma \epsilon > (m_e c^2)^2, \quad (50)$$

in head-on collisions (Romero et al. 2010b), where E_γ and ϵ are the energies of the emitted gamma-ray and the ambient photons and θ is the collision angle in the laboratory reference frame.

The attenuated luminosity $L_\gamma(E_\gamma)$ after the $\gamma-$ray travels a distance l is (Romero & Christiansen 2005)

$$L_\gamma(E_\gamma) = L^0_\gamma(E_\gamma) e^{-\tau(l, E_\gamma)} \quad (51)$$

where L^0_γ is the intrinsic coronal gamma-ray luminosity and $\tau(l, E_\gamma)$ is the optical depth. The differential optical depth is given by:

$$d\tau = (1 - \mu) n_{ph} \sigma_{\gamma\gamma} d\epsilon d\Omega dl' \quad (52)$$

where $d\Omega$ is the solid angle of the target soft photons, μ is the cosine of the angle between the gamma-ray and the arriving soft photons, l' is the path along the gamma-ray emission and n_{ph} is the black-body photon density in $\mathrm{cm}^{-3}\mathrm{erg}^{-1}\mathrm{sr}^{-1}$.

The $\gamma\gamma$ interaction cross-section $\sigma_{\gamma\gamma}$ is defined as (Gould & Scheder 1967)

$$\sigma_{\gamma\gamma}(\epsilon, E_\gamma) = \frac{\pi r_0^2}{2}(1-\beta^2)[2\beta(\beta^2-2) + (3-\beta^4) ln(\frac{1+\beta}{1-\beta})], \quad (53)$$

where r_0 is the classical radius of the electron and

$$\beta = [1 - \frac{(m_e c^2)^2}{\epsilon E_\gamma}]^{1/2}. \quad (54)$$

The companion star with radius $R_\star$ and a black-body surface temperature $T_\star$ produces a photon density at a distance $d_\star$ from the star

$$n_{ph} = \frac{2\epsilon^2}{h^3 c^3} \frac{1}{\exp(\epsilon / kT_\star)} \frac{R^2_{star}}{d^2_\star}. \quad (55)$$

In the absorption models proposed by Sierpowska-Bartosik & Torres (2008) and Dubus (2006), the geometrical parameters $d_\star$, μ and l are strongly dependent on the viewing angle θ and the orbital phase ϕ_b. In the superior conjunction, the compact object is behind the star and the orbital phase is $\phi_b = 0$. We here consider the same orbital phase that has been observed during the high energy observations for Cyg X-1 and Cyg X-3. (For more details on the geometrical conditions of the binary system and the integration extremes, see Sierpowska-Bartosik & Torres 2008 and Dubus 2006.)

We note that the pairs produced by the absorbed gamma-rays may emit predominantly synchrotron emission in the surrounding magnetic fields (Bosch-Ramon et al. 2008), but their emission is expected to be negligible compared to the other synchrotron processes of the system. We thus neglect this effect in our treatment of pair absorption (Zdziarski et al. 2014).

4 APPLICATION TO CYGNUS X-1

Cyg X-1 is a widely studied black hole binary system (Malyshev et al. 2013) at a distance of 1.86-2.2 kpc (Reid et al. 2011; Ziolkowski 2005) which is accreting from a high mass companion star orbiting around the BH with a period is 5.6 days (Gies et al. 2008). The orbit inclination is between 25° and 35° (Gies & Bolton 1986) with an eccentricity of ∼0.018 (Orosz 2011), so that one can assume an approximate circular orbit with a radius r_{orb}.

The parameters of the model for Cyg X-1 are tabulated in Table 1. The values for the first five parameters in the Table have been calculated from eqs. 1-5 above. We take for the accretion disk inner radius the value $R_X = 6R_S$, and for the extension L_X of the reconnection region (see Fig. 1), we consider the value $L_X \simeq 10R_S$ (GL05, de Gouveia Dal Pino et al. 2010a). As remarked in Section 3, the volume V of the emission region in Table 1 was calculated by considering the spherical region that encompasses the reconnection region in Figure 1.

The black hole mass has been taken from Orosz (2011). Figures 2 and 3 show the cooling rates for the different energy loss processes described in Section 3 (eqs. 10, 15, 19, 31 and 40) for electrons and protons. These are compared with the acceleration rates due to first-order Fermi acceleration by magnetic reconnection (eqs. 6 & 7) and to shock acceleration (eq. 9).

We notice that for both protons and electrons the acceleration is dominated by the first-order Fermi magnetic reconnection process in the core region. Besides, the main radiative cooling process for the electrons is synchrotron radiation, while for protons the photo-meson production ($p\gamma$ interactions) governs the loss mechanisms (Figure 3). In this case, the proper target radiation field are the photons from synchrotron emission. The intercept between the magnetic reconnection acceleration rate and the synchrotron rate in Figure 2 gives the maximum energy that the electrons can attain in this acceleration process, which is $\sim$ 10GeV. Protons on the other hand, do not cool as efficiently as the electrons and can attain energies as high as $\sim 4 \times 10^{15}$eV.

Table 1. Model parameters for Cyg X-1.

B	Magnetic field (G)	2.3×10^7
n_c	Coronal particle number density (cm^{-3})	4.5×10^{16}
T_d	Disk temperature (K)	4.4×10^7
W	Reconnection power (erg/s)	3.6×10^{36}
ΔR_X	Width of the current sheet (cm)	1.1×10^7
R_x	Inner radius of disk (cm)	2.6×10^7
L_X	Height of reconnection region (cm)	4.3×10^7
V_{vol}	Volume of emission region (cm^3)	3.5×10^{23}
d	Distance (kpc)	2
M	Mass of BH ($M_\odot$)	14.8
p	Particle power index	1.8
$R_\star$	Stellar radius (cm)	1.5×10^{12}
$T_\star$	Stellar temperature (K)	3×10^4
r_{orb}	Orbital radius (cm)	3.4×10^{12}
θ	Viewing angle (rad)	$\pi/6$

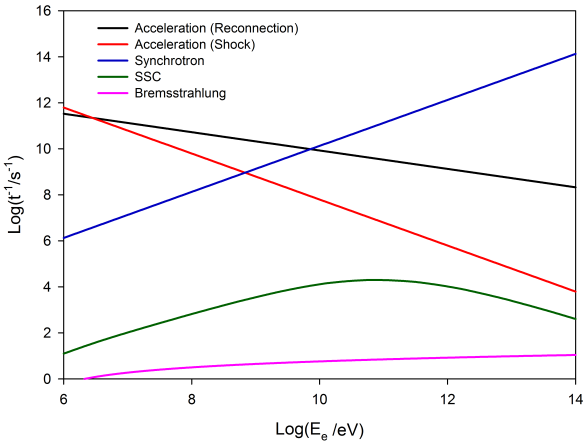

Figure 2. Acceleration and cooling rates for electrons in the nuclear region of Cyg X-1.

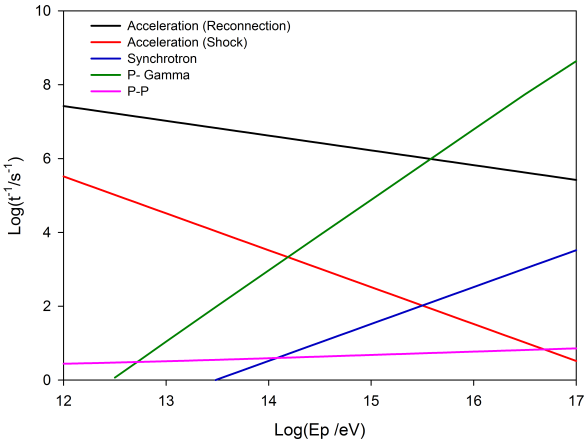

Figure 3. Acceleration and cooling rates for protons in the nuclear region of Cyg X-1.

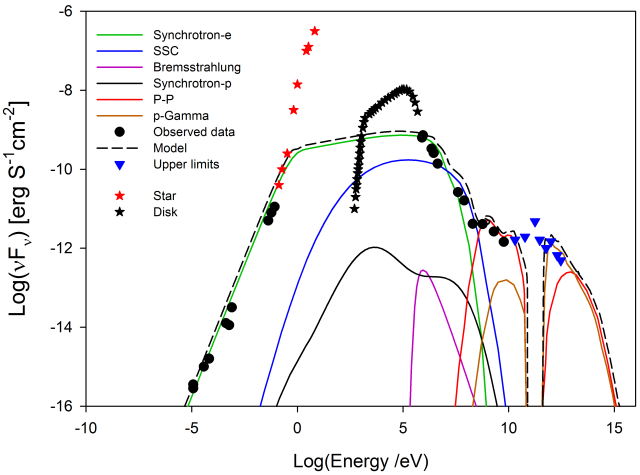

Figure 4. Calculated spectral energy distribution for Cyg X-1 using the magnetic reconnection acceleration model compared with observations. The data depicted in the radio range is from Fender et al. 2000, the IR fluxes are from Persi et al. 1980; Mirabel et al. 1996, the hard X-ray data above 20 keV are from INTEGRAL (Zdziarski et al. 2012), the soft X-ray data below 20 keV are from BeppoSAX (Di Salvo et al. 2001), the soft γ-ray data are from COMPTEL (McConnell et al. 2000, 2002), the data in the range 40 MeV- 40 GeV are measurements and upper limits from the Fermi LAT (Malyshev et al. 2013), and the data in the range 40 GeV- 3 TeV are upper limits from MAGIC (with 95% confidence level; Albert et al. 2007). The red and black stars correspond to emission from the companion star and the accretion disk, respectively, and are not investigated in the present model (see more details in the text.)

In order to reproduce the observed SED, we have calculated the non-thermal emission processes as described in Section 3 in the surrounds of the BH. Figure 4 shows the computed SED for Cyg X-1 compared with observed data. As remarked, we have also considered the gamma-ray absorption due to electron-positron pair production resulting from interactions of the gamma-ray emission in the core with the surrounding radiation field. As stressed, our calculations indicate that this process is dominated by the radiation field of the companion star. As a result, the opacity depends on the phase of the orbital motion and on the viewing angle.

The parameters employed in the evaluation of this absorption are in the last four lines of Table 1, and have been taken from Romero et al. (2010a). It has been proposed from *MAGIC* observations (Albert et al. 2007) that the gamma-ray production and absorption are maximized near the superior conjunction (Bodaghee 2013) at phase $\phi_b = 0.91$. In our calculations we considered this orbital phase for Cyg X-1.

The calculated opacity according to the equations above results in a very high energy gamma ray absorption. We find that the produced gamma-rays are fully absorbed in the energy range of 50 Gev-0.5 TeV which causes the energy gap seen in the calculated SED in Figure 4. The observed upper limits by MAGIC plotted in the diagram in this range are possibly originated outside the core, along the jet where $\gamma-$ray absorption by the stellar radiation is not important (see also Romero et al. 2010a).

We note that in Figure 4 the observed flux in radio ($10\ \mu$eV $- 0.1$ eV) and soft gamma-ray ($10^5 - 10^8$ eV) are explained by leptonic synchrotron and SSC processes according to the present model. In the range 10 MeV- 0.2

GeV, SSC is the main mechanism to produce the observed data as a result of interactions between the high energy electrons with synchrotron photons. At energies in the range 0.2 GeV - 3 TeV, neutral pion decays reproduce the observed gamma-rays. These neutral pions result from pp and $p\gamma$ interactions. In the range of 0.3 GeV- 30 GeV, pp collisions are the dominant radiation mechanism, but in the very high energy gamma-rays, interactions of relativistic hadrons (mostly protons) with scattered photons from synchrotron radiation may produce the observed flux.

The observed emission in the near infrared (0.1 eV-10 eV), represented in Figure 4 by red stars is attributed to thermal blackbody radiation from the stellar companion, and the accretion X-ray emission (1 keV-0.1 MeV) also represented in Figure 4 by dark stars, is believed to be due to thermal Comptonization of the disk emission by the surrounding coronal plasma of temperature $\sim 10^7$ K (Di Salvo et al. 2001; Zdziarski et al. 2012). For this reason, these observed data are not fitted by the coronal non-thermal emission model investigated here.

5 APPLICATION TO CYGNUS X-3

Cyg X-3 is also a high mass X-ray binary that possibly hosts a BH (Zdziarski & Mikolajewska 2013) and a Wolf-Rayet as a companion star (van Kerkwijk et al. 1992). The system is located at a distance of 7.2-9.3 kpc (Ling et al. 2009) and has an orbital period of 4.8 h and an orbital radius $\approx 3\times10^{11}$cm (Piano et al. 2012). Our model parameters for Cyg X-3 are given in Table 2. As in Cyg X-1, the values for the first five parameters were calculated from eqs. 1-5 which describe the magnetic reconnection acceleration model in the core region. We have also used for the accretion disk inner radius the value $R_X = 6R_S$ and for the extension L_X of the reconnection region the value $L_X = 10R_S$ (GL05, GPK10 and KGS14). The BH mass has been taken from Schmutz, Geballe & Schild (1996).

The cooling and acceleration rates for electrons and protons are depicted in Figures 5 and 6, respectively. The maximum electron and proton energies in both diagrams are obtained from the intercept between the acceleration rate curve and the dominant radiative loss rate curve. As in Cyg X-1, it is clear from the diagrams that acceleration by magnetic reconnection is dominating over shock acceleration in the core region. Synchrotron emission is the main mechanism to cool the electrons which may reach energies as high as $\sim$ 10GeV, while the most important loss mechanism for protons is $p\gamma$ interactions with synchrotron photons. They can be accelerated up to $\sim 4\times10^{15}$eV.

In this system, the close proximity ($R_d \approx 3\times10^{11}$cm), the large stellar surface temperature ($T_\star \sim 10^5$K), and the high stellar luminosity ($L_\star \sim 10^{39}$erg s^{-1}) of the WolfRayet star may result a considerable attenuation of the gamma-rays via $\gamma-\gamma$ pair production (Bednarek 2010). The detection of TeV gamma-rays in Cyg X-3, therefore, relies on the competition between the production and the attenuation process above.

Figure 7 shows the calculated SED compared to the observed data for this source. The gamma-ray absorption was calculated from Eq. 52, employing the UV field of the companion star which is a more significant target than the

Table 2. Model parameters for Cyg X-3.

B	Magnetic field (G)	2.1×10^7
n_c	Coronal particle number density (cm^{-3})	3.9×10^{16}
T_d	Disk temperature (K)	4.5×10^7
W	Reconnection power (erg/s)	4.5×10^{36}
ΔR_X	Width of the current sheet (cm)	1.3×10^7
R_x	Inner radius of disk (cm)	3×10^7
L_X	Height of reconnection region (cm)	5×10^7
V_{vol}	Volume of emission region (cm^3)	5.3×10^{23}
d	Distance (kpc)	8
M	Mass of BH ($M_\odot$)	17
p	Particle power index	2.2
$R_\star$	Stellar radius (cm)	2×10^{11}
$T_\star$	Stellar temperature (K)	9×10^4
r_{orb}	Orbital radius (cm)	4.5×10^{11}
θ	Viewing angle (rad)	$\pi/6$

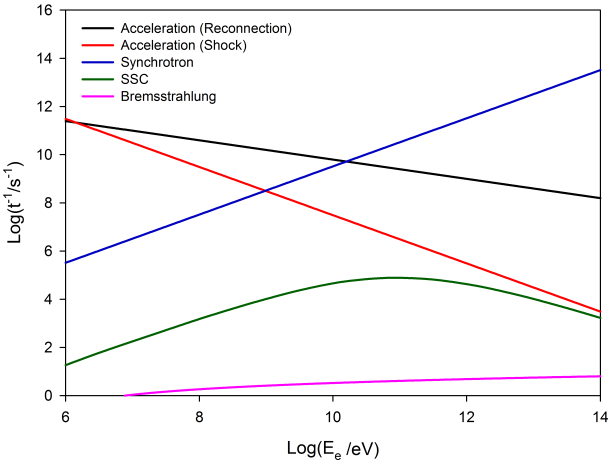

Figure 5. Acceleration and cooling rates for electrons in the core region of Cyg X-3.

radiation fields of the accretion disk and the corona (see the stellar parameters in the last four lines of Table 2 which were taken from Cherepashchuk & Moffat 1994). The orbital phase considered was $\phi_b = 0.9$, near the superior conjunction (Aleksic et al. 2010), as in Cyg X-1. The energy gap caused by this gamma-ray absorption is shown in Figure 7 in the 50GeV $-$ 0.4TeV.

The contributions of pp and $p\gamma$ interactions are the dominant ones in the high energy gamma-ray range. These processes become more relevant in the coronal region around the BH since the magnetic field there is strong and enhances the synchrotron radiation of the electrons and protons. Also the matter and photon densities are large enough in the core region, providing dense targets for pp and $p\gamma$ collisions and SSC scattering. In the energy range 10MeV $-$ 50Gev, the emission is dominated by the neutral pion decay resulting from pp inelastic collisions. Also, the resulting interactions between accelerated protons and scattered photons from synchrotron emission produce neutral pions and the gamma ray emission from these pion decays results in the tail seen in the SED for energies $\geq$ 1TeV.

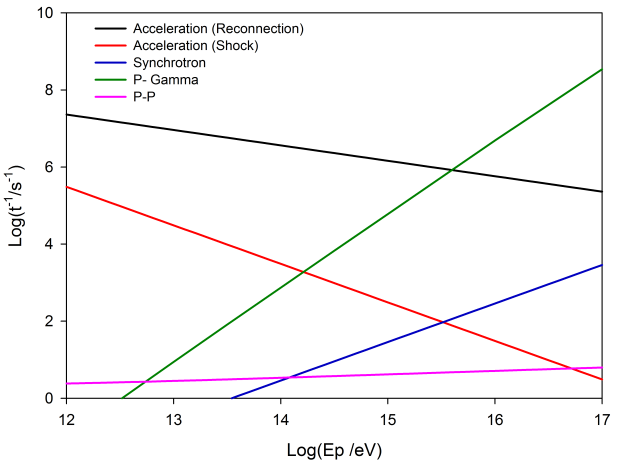

Figure 6. Acceleration and cooling rates for protons in the core region of Cyg X-3.

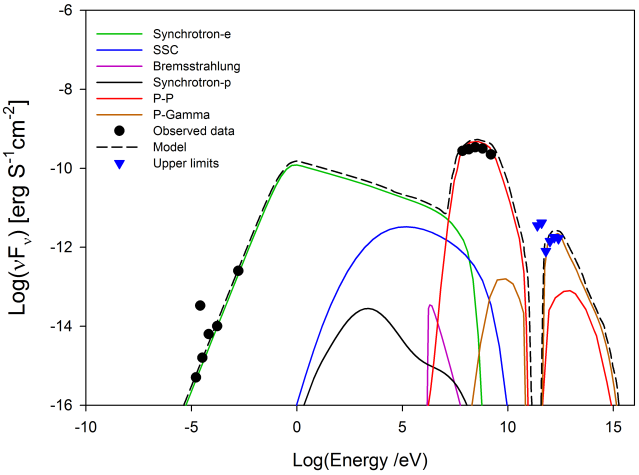

Figure 7. Spectral energy distribution for Cyg X-3. The observed radio emission is taken from AMI-LA and RATAN (Piano et al. 2012); the data in the range 50MeV to 3GeV are from AGILE-GRID (Piano et al. 2012); and the data in the range $0.2 - 3.155$TeV are from MAGIC differential flux upper limits (95% C.L.).

6 DISCUSSION AND CONCLUSIONS

The multi-wavelength detection, from radio to gamma-rays, of non-thermal energy from galactic black hole binaries (BHBs or $\mu QSRs$) is clear evidence of an efficient production of relativistic particles and makes these sources excellent nearby laboratories to investigate and review particle acceleration theory in the surrounds of BH sources in general. Based on recent studies (GL05, GPK10, KGS14), we investigated here the role of magnetic reconnection in accelerating particles in the innermost regions of these sources, applying this acceleration model to reconstruct the spectral energy distribution (SED) of the BHBs Cyg X-1 and Cyg X-3.

According to GL05, particles can be accelerated to relativistic velocities in the surrounds of the BH, near the jet basis, by a first-order Fermi process occurring in the magnetic reconnection discontinuity formed by the encounter of the magnetic field lines rising from the accretion disk with those anchored into the BH (Figure 1). This process becomes very efficient when these two magnetic line fluxes are squeezed together by enhanced disk accretion and the reconnection is fast driven e.g., by turbulence (Lazarian & Vishniac 1999; Kowal et al. 2009, 2012).

This driving mechanism has been employed to compute the magnetic reconnection power released to heat and accelerate particles in this work (see KGS14). Moreover, the first-order Fermi acceleration mechanism within reconnection sites has been tested successfully by means of 2D and 3D numerical simulations (e.g.,Kowal et al. 2011, 2012; Drake et al. 2006; Zenitani et al. 2009; Sironi & Spitkovsky 2014) and the resulting acceleration time scale is proportional to $\sim E^{0.4}$ (Kowal et al. 2012; del Valle et al. 2015). This can be compared with the typical estimated acceleration time scale in diffusive shocks for the same environment conditions $t_{acc,shock} \propto E$ (see eq. 9). We find a larger efficiency of the first mechanism in regions where magnetic discontinuities are dominant.

It should be noted that in a shock with perpendicular velocity to the magnetic field (for which particles diffuse *across* the magnetic field lines), it is predicted that the acceleration rate may be larger than that resulting from Bohm diffusion (Eq. 9) (Giacalone & Jokipii 2006; Jokipii & Giacalone 2007; Jokipii 1987; Giacalone 1998; Giacalone & Jokipii 1999). As a matter of fact, if we consider the parameters in the inner coronal regions of our BHs, a perpendicular shock could lead to acceleration rates up to 2 or 3 orders of magnitude larger than that predicted by the Bohm rate, therefore, comparable to the computed magnetic reconnection acceleration rates in Figures 2, 3, 5 and 6. However, the model we explored here assumes that the surrounds of the BH is a magnetically dominated region, which makes the development of strong shocks harder in the inner nuclear regions. Nevertheless, as stressed in Section 3, fast magnetic reconnection can release coronal mass ejections along the reconnected magnetic field lines which will then induce the formation of a shock front further out, but in this case, the shock velocity will be predominantly parallel to the large scale magnetic field lines and this explains why in Figures 2, 3, 5 and 6 we compared the magnetic reconnection acceleration rate with the Bohm shock acceleration rate which is suitable for diffusive and parallel shocks.

Even if the presence of turbulence may allow the formation of important perpendicular magnetic field components in the shock location that may affect the shock acceleration rate, it is important to remark that recent results (Lazarian & Yan 2014) have demonstrated that the divergence of the magnetic field on scales less than the injection scale of the turbulence induces superdiffusion of cosmic rays (CRs) in the direction perpendicular to the mean magnetic field. This makes the square of the perpendicular displacement to increase not with the distance x along the magnetic field, as in the case for a regular diffusion, but with x^3, for freely streaming CRs. They showed that this superdiffusion decreases the efficiency of the CR acceleration in perpendicular shocks. This superdiffusion has been also demonstrated numerically by Xu & Yan 2013 and these results suggest that

perpendicular shock acceleration efficiency is still an open question that deserves further extensive numerical testing. A perpendicular shock would still be possible for particular geometries of magnetic field lines as proposed by Jokipii 1987; Giacalone & Jokipii 1999, 2006, but this is out of the scope of the present work.

As remarked earlier, fast magnetic reconnection has been detected in space environments, like the earth magnetotail and the solar corona (see e.g., Deng & Matsumoto 2001; Su et al. 2013). Striking evidence of turbulent reconnection in the flares and coronal events at work on the Sun have been provided by observations from the *Yohkoh* and *SOHO* satellites (Priest 2001). Retinò et al. (2007) have also reported evidence of reconnection in the turbulent plasma of the solar wind downstream of the earth bow shock. They showed that this turbulent reconnection is fast and the released electromagnetic energy is converted into heating of the ambient plasma and acceleration of particles. These findings have significant implications for particle acceleration within turbulent reconnection sheets not only in the solar, but also in astrophysical plasmas, in general. Particle acceleration models due to fast magnetic reconnection have been widely explored in the solar framework. The Voyager spaceships completely failed to detect any observational evidence for shock acceleration. As the ultimate energy source in impulsive flares and in many other solar magnetic activities, fast reconnection naturally arose to explain the acceleration of the observed anomalous cosmic rays throughout the heliosphere, from the solar flares and the earth magnetosphere (e.g., Drake et al. 2006) to the heliopause (Lazarian & Opher 2009; Drake et al. 2010; Oka et al. 2010).

Considering all the relevant leptonic and hadronic radiative loss mechanisms due to the interactions of the accelerated particles with the surrounding matter, magnetic and radiation fields in the core regions of the BHBs Cyg X-1 and Cyg X-3, we compared the time scales of these losses with the acceleration time scales above and found larger energy cut-offs for particles being accelerated by magnetic reconnection than by a diffusive shock (see Figures 2 and 3 for Cyg X-1, and Figures 5 and 6 for Cyg X-3). These cut-offs have an important role in the determination of the energy distribution of the accelerated particles and therefore, in the resulting SED, and stress the potential importance of magnetic reconnection as an acceleration mechanism in the core regions of BHBs and compact sources in general.

In most astrophysical systems, synchrotron is known as a dominant mechanism to cool the electrons and for the sources studied here, its cooling rate is also larger than that of the other loss mechanisms in all electron energy range. In Cyg X-1 and Cyg X-3, electrons gain energy up to 10 GeV (Figures 2 and 5). In both cases, the achieved maximum energy are larger than the possible values obtained with Bohm-limit shock acceleration in the nuclear region. Also, for both microquasars we find that $p\gamma$ is the dominant mechanism to cool the accelerated relativistic protons in most of the investigated energy range. Only for energies below ~ 2 TeV, the *pp* inelastic collisions are more efficient. The calculated energy cut-off for protons obtained from the comparison of the $p\gamma$ cooling time with the magnetic reconnection acceleration time is 4×10^{15}eV, for both sources. In these $p\gamma$ processes, the synchrotron radiation is the dominant target photon field that interacts with the energetic protons, this because the magnetic field in the core region of these sources is relatively large, as calculated from Eq. 14.

We note that the maximum energy of the accelerated particles is not constrained only by the emission losses, but also by the size of the acceleration region, i.e., the particle Larmor radius, $r_L = E/ceB$, cannot be larger than the length scale of the acceleration zone. Considering the parameters employed in our model for both sources and ΔR_X as the length scale of the acceleration zone, we find that the maximum energy to which the protons (and electrons) can be accelerated by magnetic reconnection is $\sim 10^{17}$ eV, which is larger than the cut-off values obtained above. This value also reassures the efficiency of this acceleration process.

We have also shown that, under fiducial conditions, the acceleration model developed here is capable of explaining the multi-wavelength non-thermal SED of both microquasars Cyg X-1 and Cyg X-3. The radio emission may result from synchrotron process in both cases.

The observed soft gamma-rays from Cyg X-1 are due to synchrotron and IC processes. The target photons for the IC come mainly from synchrotron emission (SSC). Neutral Pion decay resulting from *pp* inelastic collisions may produce the high energy gamma rays in both systems, while the very high energy (VHE) gamma rays are the result of neutral pion decay due to photo-meson production ($p\gamma$) in the core of these sources.

The importance of the $\gamma - \gamma$ absorption due to interactions with the photon field of the companion star for electron-positron pair production has been also addressed in our calculations. According to our results, the observed gamma-ray emission in Cyg X-1 in the range $5 \times 10^{10} - 5 \times 10^{11}$eV (see inverted blue triangles in Figure 4) cannot be produced in its core region (see also Romero et al. 2010a). In the case of Cyg X-3, we have found that the emission in the range of $50\text{GeV} - 0.4\text{TeV}$ (see inverted blue triangles in Figure 7) is also fully absorbed in the core region by the same process. This suggests that in both sources, this emission is produced outside the core, probably along the jet, since at larger distances from the core the gamma ray absorption by the stellar companion decreases substantially. In fact, this is what was verified by Zhang, Xu & Lu (2014) in the case of Cyg X-1.

Other authors have proposed alternative scenarios to the one discussed here. The models of Piano et al. (2012), for instance, which were based on particle acceleration near the compact object and on propagation along the jet, indicate that the observed gamma-ray ≤ 10 GeV in Cyg X-3 could be produced via leptonic (inverse Compton) and hadronic processes (*pp* interactions). However, they have no quantitative estimates for the origin of the VHE gamma-ray upper limits at $\geq$0.1 TeV obtained by *MAGIC*. Sahakyan et al. (2013), on the other hand, assumed that the jet of Cyg X-3 could accelerate both leptons and hadrons to high energies and the accelerated protons escaping from the jet would interact with the hadronic matter of the companion star producing $\gamma-$rays and neutrinos. However, their model does not provide proper fitting in the TeV range either.

In the case of Cyg X-1, Zhang, Xu & Lu (2014) have employed a leptonic model to interpret recent Fermi LAT measurements also as due to synchrotron emission but produced along the jet and to Comptonization of photons of

the stellar companion. The TeV emission in their model is attributed to interactions between relativistic electrons and stellar photons via inverse Compton scattering. According to them this process could also explain the *MAGIC* upper limits in the range of $50\mathrm{GeV}-0.5\mathrm{TeV}$, i.e., the band gap in Figure 4. However, unlike the present work where we obtained a reasonable match due to $p\gamma$ interactions, their model is unable to explain the observed upper limits by *MAGIC* in the very high energy gamma-ray tail.

Also with regard to Cyg X-1, we should note that the detection of strong polarized signals in the high-energy range of 0.4-2 MeV by Laurent et al. (2011) and Jourdain et al. (2012) suggests that the optically thin synchrotron emission of relativistic electrons from the jet may produce soft gamma-rays. There are indeed some theoretical models that explain the emission in this range by using a jet model (Zdziarski et al. 2012; Malyshev et al. 2013; Zdziarski et al. 2014; Zhang, Xu & Lu 2014). Nevertheless, contrary to this view, Romero, Vieyro & Chaty (2014) argue that the MeV polarized tail may be originated in the coronal region of the core without requiring the jet. This study is therefore, consistent with the present model as it supports the coronal nuclear region for the origin of the non-thermal emission.

The results above clearly stress the current uncertainties regarding the region where the HE and VHE emission are produced in these compact sources. This work has tried to shed some light on this debate focussing on a core model with a magnetically dominated environment surrounding the BH, but a definite answer to this question should be given by much higher resolution and sensitivity observations which may be achieved in near future with the forthcoming Cherenkov Telescope Array (CTA) (Actis et al. 2011; Acharya et al. 2013; Sol et al. 2013).

We should also stress that there are two possible interpretations for the lack of clear evidence of detectable TeV emission in Cyg X-1 and Cyg X-3. On one hand, there may be a strong absorption of these photons by the ultraviolet (UV) radiation of the companion star (through the photon-photon process). On the other hand, the lack of emission may be due to the limited time of observation (Sahakyan et al. 2013). In our model, we verified that neutral pion decays due to $p\gamma$ interactions at the emission region close enough to the central black hole, near the jet basis, could produce TeV gamma-rays. Because of the high magnetic field near the black hole, a large density synchrotron radiation field produced there could be a target photon field for the photo-meson production. These results predict that a long enough observation time and higher sensitivity would allow to capture substantial TeV γ-ray emission from these microquasars. This may be also probed by the CTA.

A final remark is in order. To derive the SEDs of the sources investigated here, we have assumed a nearly steady-state accelerated particle energy distribution at the emission zone. This assumption is valid as long as acceleration by fast magnetic reconnection is sustained in the inner disk region, or in other words, as long as a large enough disk accretion rate is sustained in order to approach the magnetic field lines rising from the accretion disk to those anchored into the BH. In microquasars, this should last no longer than the time the system remains in the outburst state, normally ranging from less than one day to several weeks.

ACKNOWLEDGEMENTS

This work has been partially supported by grants from the Brazilian agencies FAPESP (2006/50654-3, and 2011/53275-4), CNPq (306598/2009-4) and CAPES. The authors are also indebted to Helene Sol for her useful comments on this work. EMGDP particularly thanks her kind hospitality during her visit to the Observatoire de Paris-Meudon.

REFERENCES

Acharya, B. S., Actis, M., Aghajani, T., et al. 2013, Astroparticle Physics, 43, 3
Actis, M., Agnetta, G., Aharonian, F., et al. 2011, Experimental Astronomy, 32, 193
Aharonian, F. A., & Atoyan, A. M. 2000, A&A, 362, 937
Albert, J., Aliu, E., Anderhub, H., et al. 2007, ApJ, 665, L51
Aleksić, J., Antonelli, L. A., Antoranz, P., et al. 2010, ApJ, 721, 843
Atoyan, A. M., & Dermer, C. D. 2003, ApJ, 586, 79
Atwood, W. B., Abdo, A. A., Ackermann, M., et al. 2009, ApJ, 697, 1071
Bednarek, W. 2010, MNRAS, 406, 689
Berezinskii, V. S. 1990, Astrophysics of Cosmic Rays, North-Holland, Amsterdam
Biskamp, D., Schwarz, E., & Drake, J. F. 1997, Physics of Plasmas, 4, 1002
Blumenthal, G. M., & Gould, R. J. 1970, Rev. Mod. Phys., 42, 237
Bodaghee, A., Tomsick, J. A., Pottschmidt, K., et al. 2013, ApJ, 775, 98
Bosch-Ramon, V., Romero, G. E., & Paredes, J. M. 2005a, A& A, 429, 267
Bosch-Ramon, V., Aharonian, F. A., & Paredes, J. M. 2005b, A& A, 432, 609
Bosch-Ramon, V., Khangulyan, D., Aharonian, F. A. 2008, A&A, 489, L21
Bulgarelli, A., Pittori, C., Lucarelli, F., et al. 2010. Atel, 2512
Čemeljić, M., Shang, H., & Chiang, T. Y. 2013, ApJ, 768, 5
Cerutti, B., Dubus, G., Malzac, J., et al. 2011, A&A 529, A120
Cerutti, B., Werner, G. R., Uzdensky, D. A., Begelman, M. C. 2013, ApJ., 770, 147C
Cerutti, B., Werner, G. R., Uzdensky, D. A., Begelman, M. C. 2014, ApJ., 782, 104C
Cherepashchuk, A., Moffat, A. 1994, ApJ, 424, 53
Cho, J. and Lazarian, A. 2014, ApJ, 780, 30
de Gouveia Dal Pino, E. M. & Lazarian, A. 2005, Astronomy and Astrophysics, 441, 845
de Gouveia Dal Pino, E. M., Piovezan, P. P. & Kadowaki, L. H. S. 2010a, Astronomy and Astrophysics, 518, A5
de Gouveia Dal Pino, E. M., Kowal, G. & Lazarian, A. 2014, 8th International Conference of Numerical Modeling of Space Plasma Flows (ASTRONUM 2013), ASP Conf. series, 488, 8
de Gouveia Dal Pino, E. M., & Kowal, G. 2015, in Magnetic Fields in Diffuse Media (eds. A. Lazarian, E. M. de Gouveia Dal Pino, C. Melioli), Astrophysics and Space Science Library, 407, 373

del Valle, M. V., Romero, G. E., Luque-Escamilla, P. L., Martí, J., & Ramón Sánchez-Sutil, J. 2011, ApJ, 738, 115
del Valle, M. V., et al. 2015, Submitted
Deng, X. H. & Matsumoto, H. 2001, Nature 410, 557
Dexter, J., McKinney, J. C., Markoff, S., & Tchekhovskoy, A. 2014, MNRAS, 440, 218
Di Salvo, T., Done, C., Zycki, P. T., Burderi, L. & Robba, N. R. 2001, ApJ, 547, 1024
Drake, J. F., Swisdak, M., Che, H. and Shay, M. A. 2006, Nature, 443, 553D
Drake, J. F., Opher, M., Swisdak, M. and Chamoun, J. N. 2010, ApJ,709, 963
Drury, L. 2012, MNRAS, 422, 2474D
Dubus, G. 2006, A&A 451,9
Eyink, G. L., Lazarian, A., & Vishniac, E. T. 2011, ApJ, 743, 51
Fender, R. P., Pooley, G. G., Durouchoux, P., Tilanus, R. P. J.,& Brocksopp, C. 2000, MNRAS, 312, 853
Gaisser, T. K. 1990, Cosmic Rays and Particle Physics, Cambridge University Press
Giacalone, J. 1998, Space Sci. Rev., 83, 351
Giacalone, J., & Jokipii, J. R. 1999, ApJ, 520, 204
Giacalone, J., & Jokipii, J. R. 2006, JPhCS, 47, 160
Giannios, D. 2010, MNRAS, 408, L46
Gies, D. R., & Bolton, C. T. 1986, ApJ, 304, 371
Gies, D. R., et al. 2008, ApJ, 678, 1237
Ginzburg, V. L., & Syrovatskii, S. I. 1995, ARA&A, 3, 297
Gordovskyy, M., Browning, P. K., & Vekstein, G. E. 2010, ApJ, 720, 1603
Gordovskyy, M., & Browning, P. K. 2011, ApJ, 729, 101
Gould, R. J., & Schreder, G. P. 1967, PhRv, 155, 1404
Hjellming, R. M., Rupen, M. P. 1995, Nature, 375, 464
Huang, C. Y., Wu, Q., & Wang, D. X. 2014, MNRAS, 440, 965
Igumenshchev, I. V. 2009, ApJL, 702, L72
Jokipii, J. R. 1987, Apj, 313, 842
Jokipii, J. R., & Giacalone, J. 2007, Apj, 660, 336
Jourdain, E., Roques, J. P., Chauvin, M.,& Clark, D. J. 2012, ApJ, 761, 21
Kadowaki, L. H. S., de Gouveia Dal Pino, E. M. & Singh, C. B. 2015, ApJ (accepted), arXiv:1410.3454
Kelner, S. R., Aharonian, F. A., & Bugayov, V. V. 2006, Phys.Rev. D, 74, 0330108
Kelner, S. R., Aharonian, F. A., & Bugayov, V. V. 2009, Phys.Rev. D, 79, 039901
Kotera, K., & Olinto, A. V. 2011, ARA&A, 49, 119
Kowal, G., Lazarian, A., Vishniac, E. T., Otmianowska-Mazur, K. 2009, ApJ, 700, 63
Kowal, G., de Gouveia Dal Pino, E. M., Lazarian, A. 2011, The Astrophysical Journal, 735, 102
Kowal, G., de Gouveia Dal Pino, E. M., Lazarian, A. 2012, Physical Review Letters, 108, 241102
Laurent, P., Rodriguez, J., Wilms, J., Cadolle Bel, M. and Pottschmidt, K.,& Grinberg,V. 2011, Sci, 332, 438
Lazarian, A., & Vishniac, E. T. 1999, The Astrophysical Journal, 517, 700
Lazarian, A., & Opher, M. 2009, ApJ, 703, 8
Lazarian, A., & Desiati, P. 2010, ApJ, 722, 188
Lazarian, A., Vlahos, L., Kowal, G., Yan, H., Beresnyak, A. & de Gouveia Dal Pino, E. M. 2012, Space Science Reviews, 173, 557
Lazarian, A., & Yan, H. 2014, ApJ, 784, 38
Leão, M. R. M., de Gouveia Dal Pino, E. M., Santos-Lima, R., & Lazarian, A. 2013, ApJ, 777, 46
Lin, R. P., & Hudson, H. S. 1971, SoPh, 17, 412
Ling, Z., Zhang, S. N. & Tang, S. 2009, ApJ, 695, 1111
Liu, B. F., Mineshige, S., & Ohsuga , K. 2003, ApJ, 587, 571
Lorentz, E. 2004, NewAR, 48, 339
Loureiro, N. F., Schekochihin, A. A., & Cowley, S. C. 2007, Physics of Plasmas, 14, 100703
Lyubarsky, Y., & Liverts, M. 2008, ApJ, 682, 1436
Malyshev, D., Zdziarski, A., & Chernyakova, M. 2013, MNRAS, 434, 2380
Malzac, J., Petrucci, P. O., & Jourdain, E. et al. 2006, A&A, 448, 1125
McConnell, M. L. et al. 2000, ApJ, 543, 928
McConnell, M. L. et al. 2002, ApJ, 572, 984
McKinney, J. C., Tchekhovskoy, A., & Blandford, R. D. 2012, MNRAS, 423, 3083
Merloni, A., Heinz, S., & di Matteo, T. 2003, MNRAS, 345, 1057
Mirabel, I. F., & Rodriquez, L. F. 1994, Nature, 371, 46
Mirabel, I. F., Claret, A., Cesarsky, C. J., Boulade, O.,& Cesarsky, D. A. 1996, A&A, 315, L113
Neronov, A., & Aharonian, F. A. 2007, ApJ, 671, 85
Oka, M., Phan, T. D., Krucker, S., Fujimoto, M., & Shinohara, I. 2010, ApJ, 714, 915
Orosz, A. 2011, ApJ, 742, 84
Parker, E. N. 1979, Oxford, Clarendon Press; New York, Oxford University Press, 1979, 858 p.
Persi, P., Ferrari-Toniolo, M., Grasdalen, G. L.,& Spada, G. 1980, A&A, 92, 238
Piano, G., et al. 2012, A & A 545, A110
Priest, E. R. 2001, Earth Planets Space, 53, 483
Reid, M. J., McClintock, J. E., Narayan, R., Gou, L., Remillard, R. A., & Orosz, J. A. 2011, ApJ, 742, 83
Remillard, R. A., McClintock, J. E. 2006, ARA&A, 44, 49R
Retinò, A., Sundkvist, D., Vaivads, A., et al. 2007, Nature Physics, 3, 236
Reynoso, M. M., Medina, M. C. and Romero, G. E. 2011, A&A 531, A30, 201
Romanova, M. M., Ustyugova, G. V., Koldoba, A. V., & Lovelace, R. V. E. 2002 ApJ, 578, 420
Romanova, M. M., Ustyugova, G. V., Koldoba, A. V., & Lovelace, R. V. E. 2011, MNRAS, 416, 416
Romero, G. E., Torres, D. F., Kaufman Bernardo, M. M., & Mirable, I. F. 2003, A&A, 410,L1
Romero, G. E., Christiansen, H. R., Orellana, M. 2005, apj 632,1093, 2005
Romero, G., E., del Valle, M., V., & Orellana, M. 2010a, A&A 518, A12
Romero, G. E., Vieyro, F. L. and Vila, G. S. 2010b, A&A 519, A109
Romero, G. E., Vieyro, F. L.,& Chaty, S. 2014, A&A 562, 7
Sabatini, S., Striani, E., Verrecchia, F., et al. 2010a, ATEL, 2715
Sabatini, S., Tavani, M., Striani, E., et al. 2010b, ApJL, 712, L10
Sabatini, S., Tavani, M., Coppi, P., et al. 2013, ApJ, 766, 83
Sahakyan, N., Piano, G., Tavani, M. 2013, arXiv:1310.7805
Santos-Lima, R., Lazarian, A., de Gouveia Dal Pino, E. M.,

& Cho, J. 2010, ApJ, 714, 442
Santos-Lima, R., de Gouveia Dal Pino, E. M., & Lazarian, A. 2012, ApJ, 747, 21
Santos-Lima, R., de Gouveia Dal Pino, E. M., & Lazarian, A. 2013, MNRAS, 429, 3371
Schmutz, W., Geballe, T. R., & Schild, H. 1996, A&A, 311, L25
Shay, M. A., Drake, J. F., Denton, R. E., & Biskamp, D. 1998, JGR, 103, 9165
Shay, M. A., Drake, J. F., Swisdak, M., & Rogers, B. N. 2004, Physics of Plasmas, 11, 2199
Shibata, K., & Tanuma, S. 2001, Earth, Planets, and Space, 53, 473
Sierpowska-Bartosik, A. & Torres, D. F. 2008, APh, 30, 239
Singh, C. B., de Gouveia Dal Pino, E. M. & Kadowaki, L. H. S. 2015, ApJ, 799, L20
Sironi, L., & Spitkovsky, A. 2014, ApJ, 783, 21
Soker, N. 2010, ApJL, 721, L189
Sol, H., Zech, A., Boisson, C., et al. 2013, Astroparticle Physics, 43, 215
Somov, B. V. 2012,*Plasma Astrophysics, Part I: Fundamentals and Practice*, Astrophysics and Space Science Library, 391
Spitzer, L. 1962, Physics of Fully Ionized Gases, New York: Interscience (2nd edition), 1962
Spruit, H. C. 1988, A&A, 194, 319
Stecker, F. W. 1968, Phys. Rev. Lett., 21, 1016
Su, Y., Veronig, A. M., Holman, G. D., Dennis, B. R., Wang, T., Temmer, M., & Gan, W. 2013, NatPh, 9, 489
Tavani, M., et al. 2009, A& A, 502, 99
Tchekhovskoy, A., Narayan, R., & McKinney, J. C. 2011, MNRAS, 418, L79
Tingay, S. J., et al. 1995, Nature, 374, 141
Uzdensky, D. A. 2011, Space Science Reviews, 160, 45
Uzdensky, D. A., & Spitkovsky, A. 2014, ApJ, 780, 3
van Kerkwijk, M. H., et al. 1992, Nature, 355, 703
Vila, G. S. and Aharonian, F. 2009, Asociaon Argentina de Astronomia- Book Series, AAABS, Vol. 1, 2009
Xu, S., & Yan, H. 2013, ApJ, 779, 140
Yamada, M., Kulsrud, R., & Ji, H. 2010, Reviews of Modern Physics, 82, 603
Yamada, M., Jongsoo, Y., Jonathan, J. A., Hantao, J., Russell M. K. & Clayton, E. M. 2014, Nature Communications 5, 4774
Zanni, C., & Ferreira, J. 2009, AAP, 508, 1117
Zanni, C., & Ferreira, J. 2013, AAP, 550, A99
Zdziarski, A. A., Lubinski, P.,& Sikora, M. 2012, MNRAS, 423, 663
Zdziarski, A. A., Mikolajewska, J., & Belczynski, K. 2013, MNRAS, 429, L104
Zdziarski, A. A., Stawarz, L., Pjanka, H. C., Bhatt, P.& Sikora, M. 2014, MNRAS, 440, 2238Z
Zenitani, S. and Hoshino, M. 2001, ApJ, 562L, 63Z
Zenitani, S., Hesse, M. & Klimas, A. 2009, ApJ, 696, 1385Z
Zhang, L., Chen, S. B. & Fang, J. 2008, The astrophysical Journal, 676:1210-1217
Zhang, B., & Yan, H. 2011, ApJ, 726, 90
Zhang, S. 2013, Fron. Phys., 8(6), 630
Zhang, J., Xu, B. & Lu, J. 2014, ApJ, 788, 143
Zharkova, V. V., Arzner, K., Benz, A. O., et al. 2011, SSR, 159, 357
Ziolkowski, J. 2005, MNRAS, 358, 851

APPENDIX A: PARTICLE ENERGY DISTRIBUTION FUNCTION

The relativistic particles in the core region surrounding the BH may be accelerated up to relativistic energies by a first-order Fermi process occurring within the magnetic reconnection site. The injection and cooling of the accelerated particles occurs mainly in the coronal region around the black hole (see Figure 1). We parametrize the isotropic injection function (in units of $\mathrm{erg}^{-1}\mathrm{cm}^{-3}\mathrm{s}^{-1}$) as a power law with a high energy cut-off,

$$Q(E) = Q_0 E^{-p} exp[-E/E_0] \tag{A1}$$

with $p > 0$ and E_0 is the cut-off energy. The normalization constant Q_0 is calculated from the total power injected in each type of particle

$$L_{(e,p)} = \int_{V_{vol}} d^3r \int_{E^{min}}^{E^{max}} dE\ E\ Q_{(e,p)}(E) \tag{A2}$$

where $L_{(e,p)}$ is the fraction of the magnetic reconnection power that accelerates the electrons and protons (see eq. 1 in the text). The injection particle spectrum is modified in the emission region due to energy losses. We assume that the minimum energy of the particles is given by mc^2, where m is the rest mass of the particle[8] and the maximum energy that the primary particles can attain is fixed by the balance of acceleration and the energy losses. Particles can gain energy up to a certain value E_{max} for which the total cooling rate equals the acceleration rate.

The kinetic equation that describes the general evolution of the particle energy distribution $N(E,t)$ is the Fokker-Planck differential equation (Ginzburg & Syrovatskii 1995). We here use a simplified form of this equation. We employ the one-zone approximation to find the particle distribution, assuming that the acceleration region is spatially thin enough, so that we can ignore spatial derivatives in the transport equation. Physically, this means that we are neglecting the contributions to $N(E)$ coming from other regions than the magnetic reconnection region in the inner accretion disk zone in the surrounds of the BH. We consider a steady-state particle distribution which can be obtained by setting $\frac{\partial N}{\partial t} = 0$ in the Fokker-Planck differential equation, so that the particle distribution equation is

$$N(E) = |\frac{dE}{dt}|^{-1} \int_E^{\infty} Q(E) dE. \tag{A3}$$

Here $-\frac{dE}{dt} \equiv E t_{cool}^{-1}$. It is very interesting to note that if the energy losses are proportional to the particle energy ($\frac{dE}{dt} \propto E$), $N(E)$ does not change the injection spectrum and $N(E) \propto E^{-p}$, as in the pp inelastic collisions or Bremsstrahlung cool processes. In such loss mechanisms like synchrotron and IC scattering, in the Thomson regime, the $N(E)$ is steeper because in these cases $\frac{dE}{dt} \propto E^2$ and $N(E) \propto E^{-(p+1)}$.

[8] We note that the calculation of the emitted flux is little affected by the choice of the minimum energy of the particle spectrum.

The spectrum would be harder if dE/dt were constant as for ionization losses, $N(E) \propto E^{-(p-1)}$. In the case of IC scattering in the Klein-Nishina limit, $\frac{dE}{dt} \propto E^{-1}$ and so, the spectrum is even harder and $N(E) \propto E^{-(p-2)}$.

This paper has been typeset from a TEX/ LATEX file prepared by the author.